Supplementary Information

Combined Effect of High Voltage and Large Li-ion Flux on Decomposition of Li_6PS_5Cl

Deye Sun[†a,b,c,d], Wenru Li[†a,b,c], Yantao Wang[†a,b,c], Jiangwei Ju[a,b,c], Pengxian Han[a,b,c], Shanmu Dong[*a,b,c], Jun Ma[*a,b,c], Guanglei Cui[*a,b,c,d]

a Qingdao Industrial Energy Storage Research Institute, Qingdao Institute of Bioenergy and Bioprocess Technology, Chinese Academy of Sciences, Qingdao 266101, China

b Shandong Energy Institute, Qingdao 266101, China

c Qingdao New Energy Shandong Laboratory, Qingdao 266101, China

d Center of Materials Science and Optoelectronics Engineering, University of Chinese Academy of Sciences, Beijing 100049, China.

† D.S., W. L., and Y. W., contributed equally to the work.

* Corresponding author. E-mail address: dongsm@qibebt.ac.cn; majun@qibebt.ac.cn; cuigl@qibebt.ac.cn.

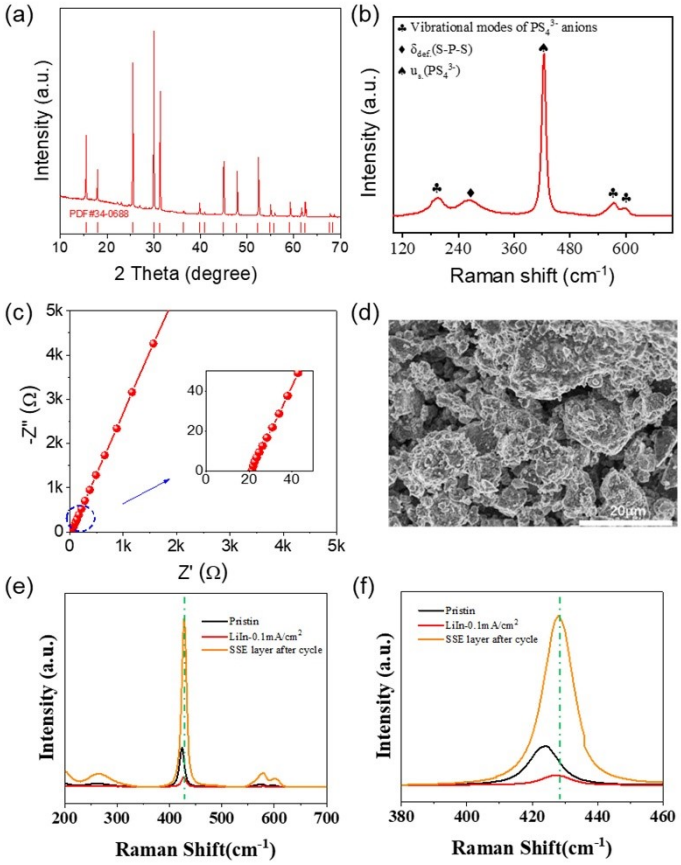

Figure S1. (a) XRD, (b) Raman, (c) Impendence spectrums and (d) SEM image of the as prepared LPSCl powder. The thickness (*L*) and contact area (*S*) of the electrolyte sheet are 0.035 cm and 0.785 cm^2, respectively. (e) The Raman spectrums of LPSCl on diffternt state. The black line represents the initial state of LPSCl. The red line and the orange line respectively represent LPSCl in the electrode-surface region and the electrolyte-layer region after the LiIn|LPSCl|LiIn battery has undergone 10 cycles at a current density of 0.1 mA cm^{-2}. (f) Local magnification around 400 cm^{-1}.

The XRD pattern shown in Figure S1a demonstrates the prepared LPSCl powder possessing a well-formed crystal structure with the *F-43* space group. In Figure S1b, the peaks at 199, 272, 425, 573, and 600 cm^{-1} of the Raman spectrum are all attributed to vibrational modes of PS_4^{3-} within LPSCl, the assignment of which are shown in Table S1. And the ionic conductivity of the LPSCl after ball-milling was found to be ~2×10^{-3} S cm^{-1}, which is calculated based on the impedance spectrum shown in Figure S1c. In Figure S1d, the SEM image of LPSCl shows secondary aggregates composed of sheet-like particles.

Table S1. Peak assignments for the pristine LPSCl.

Frequency (cm^{-1})	**Assignment**	**Ref**
196	PS_4^{3-}	[1-3]
266	δ_{def}(S−P−S) in PS_4^{3-}	[3, 4]

423	$\upsilon_s(PS_4^{3-})$ in PS_4^{3-}	[3, 5-8]
573	PS_4^{3-}	[1, 3]
600	PS_4^{3-}	[1, 3]

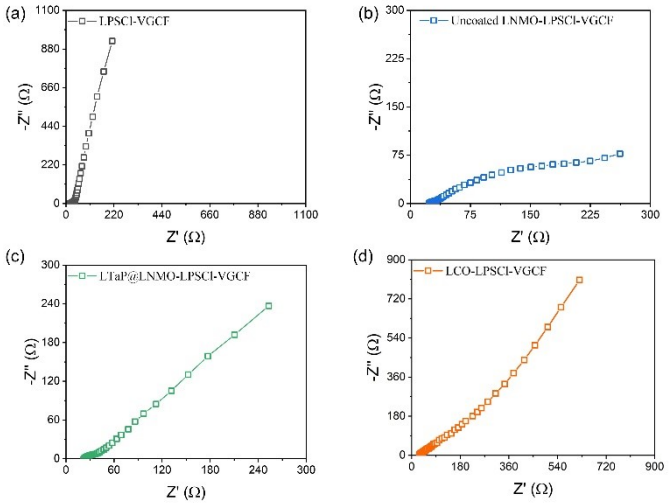

Figure S2. The EIS curves of (a) LPSCl-VGCF | LPSCl | LiIn, (b) uncoated LNMO-LPSCl-VGCF | LPSCl | LiIn, (c) LTaP@LNMO-LPSCl-VGCF | LPSCl | LiIn and (d) LCO-LPSCl-VGCF | LPSCl | LiIn cells, respectively. The batteries used for EIS measurement are newly assembled.

Figure S2a shows the impedance spectrum of the all-solid-state battery using the composite cathode of LPSCl and VGCF without the positive active material. And Figures S2b–c display the impedance spectra of all-solid-state batteries composed of the LNMO composite cathodes before and after coated with LTaP. It can be seen that the construction of the LTaP coating layer significantly reduces the interfacial impedance and greatly improves the charge-discharge performance of the all-solid-state battery. Due to the excellent electronic and ionic conductivity, the LCO all-solid-state battery shows a smaller impedance value, as shown in Figure S2d.

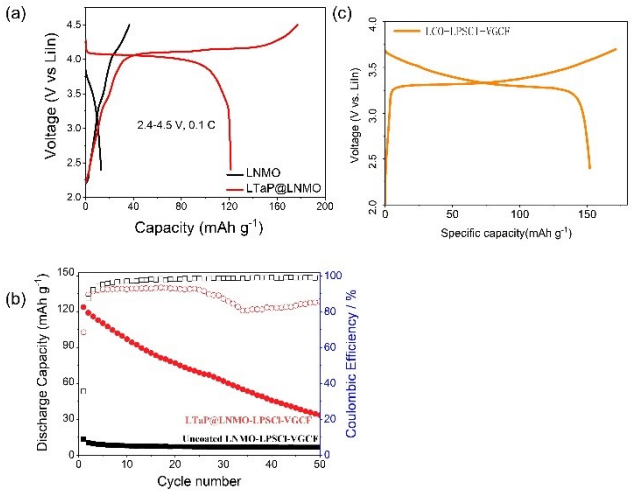

Figure S3. (a) The initial galvanostatic charge/discharge curves of uncoated LNMO-LPSCl-VGCF | LPSCl | LiIn cell and LTaP@LNMO-LPSCl-VGCF | LPSCl | LiIn cell. (b) The cycling tests LNMO-LPSCl-VGCF | LPSCl | LiIn cell and LTaP@LNMO-LPSCl-VGCF | LPSCl | LiIn cell measured at 0.1 C and 30 ℃. (c) The initial galvanostatic charge/discharge curves of LCO-LPSCl-VGCF | LPSCl | LiIn cell.

Figure S3a shows that after the LTaP coating treatment, the electrochemical performance of LNMO was significantly improved. The initial charge and discharge specific capacity of uncoated LNMO increased from 36.6 mAh g^{-1} and 13 mAh/g to 177 mAh g^{-1} and 121.4 mAh g^{-1} after coating, respectively. As can be seen from Figure S3b, although the specific capacity of the LNMO@LTaP-based all-solid-state battery is attenuated sharply during the cycle, it is significantly better than the electrochemical performance of the LNMO-based all-solid-state battery. The constructed LTaP coating layer has relatively poor electronic conductivity and high lithium ion conductivity. As an artificial SEI passivation layer, it may alleviate the influence of the space charge layer at the interface caused by different lithium chemical potentials, and reduces the lithium migration barrier at the LNMO/LPSCl interface. Figure S3c shows that due to the high electrical conductivity, the uncoated LCO sample also exhibits excellent charge-discharge performance in the all-solid-state battery, with a specific discharge capacity of over 150 mAh g^{-1}. This indirectly demonstrates its ability to provide ion flow during the charge-discharge process.

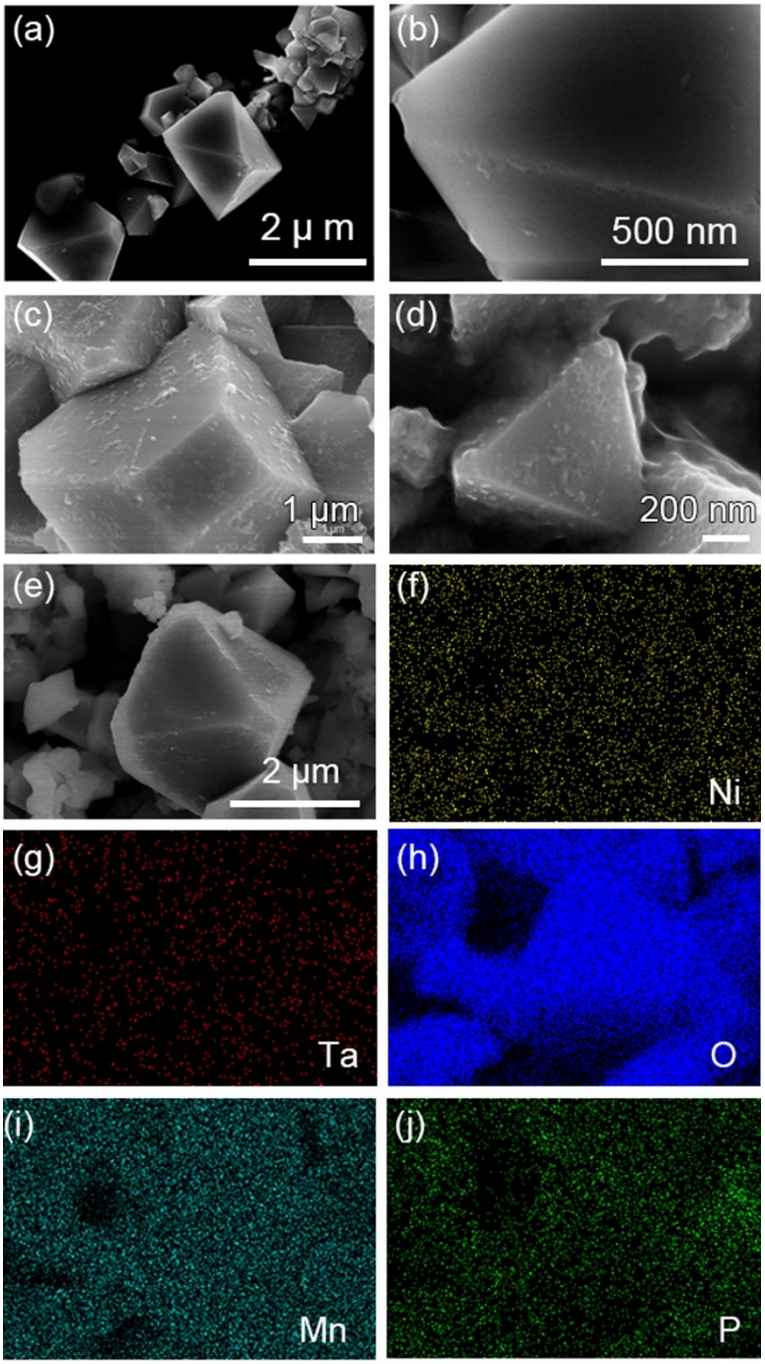

Figure S4. Characterizations of LNMO before and after LTaP coating treatment. (a, b) Typical SEM images of LNMO. (c, d) Typical SEM images of LTaP@LNMO. (e-j) EDS elemental mappings of LTaP@LNMO.

For spinel materials, their unit cell structure features a face-centered cubic close-packing of oxygen ions. Commonly, only three types of crystal planes (100), (110), and (111) are exposed. Typical SEM images show an octahedron morphology, as depicted in the Figure S4. Among them, the (111)

crystal plane has the regular octahedron fully exposed, while the newly exposed plane of the truncated octahedron is the (100) plane. As can be seen from the Figure S4, compared with the smooth surface of the original material, the surface of the coated LNMO becomes significantly rougher. The mapping results show that the characteristic elements of the coating material, Ta and P, are uniformly distributed on the surface of LNMO.

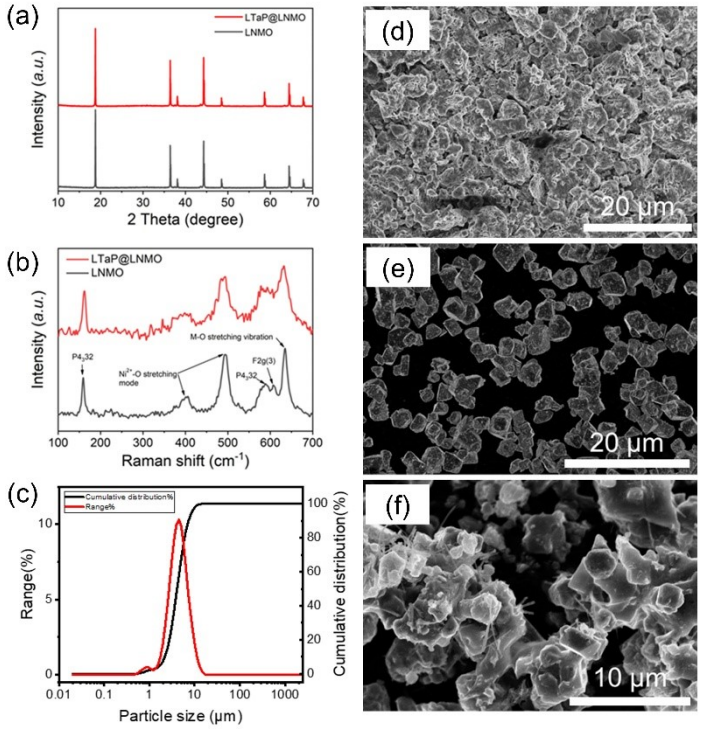

Figure S5. (a) XRD and (b) Raman spectra of LNMO and LTaP@LNMO cathode materials. (c) Particle size distribution of LNMO. Typical SEM images of (d) LNMO@LTaP, (e) the mixture of LPSCl, LNMO@LTaP and VGCF.

Table S2. Peak assignments for the pristine $LiNi_{0.5}Mn_{1.5}O_4$.

Frequency (cm^{-1})	**Assignment**	**Ref**
159	The features of $P4_332$ structure	[9]
405.8	Ni^{2+}–O stretching mode	[9-11]
493		
589	The F2g(3) splits in two components, characteristic of the ordered structure ($P4_332$)	[9; 10]
607		
634	M–O stretching vibration of MnO6 groups, belong to Ag mode	[9-11]

To study the crystal structure of the $LiMn_{1.5}Ni_{0.5}O_4$ coated by LTaP, the XRD patterns of the $LiMn_{1.5}Ni_{0.5}O_4$ samples before and after coating treatment were analyzed. The XRD results are shown in Figure S5a. The sharp diffraction peaks indicate that all the samples have good crystallinity. And both samples exhibit typical diffraction peaks corresponding to spinel structure. Combining with the Raman characterization of LNMO in Figure S5b, we can determine that the purchased LNMO has a $P4_332$ space group and it is an ordered structure. In Figure S5a, the weak impurity peaks emerging at 38.2°, 43.6°, 48.6°, 58.8°, 64.6° and 68° belong to the $Li_xNi_{1-x}O$ rock-salt phase or certain non-stoichiometric compounds of $LiMn_2O_4$. Since this raw material is produced by the manufacturer through the high-temperature solid-state method, the formation of a small amount of impurity phases is inevitable during the high-temperature sintering process. Meanwhile, from the comparison of XRD patterns before and after coating, we can observe that the peak positions of LNMO remain unchanged after coating. This indicates that the coating material does not significantly alter the crystal structure of LNMO.

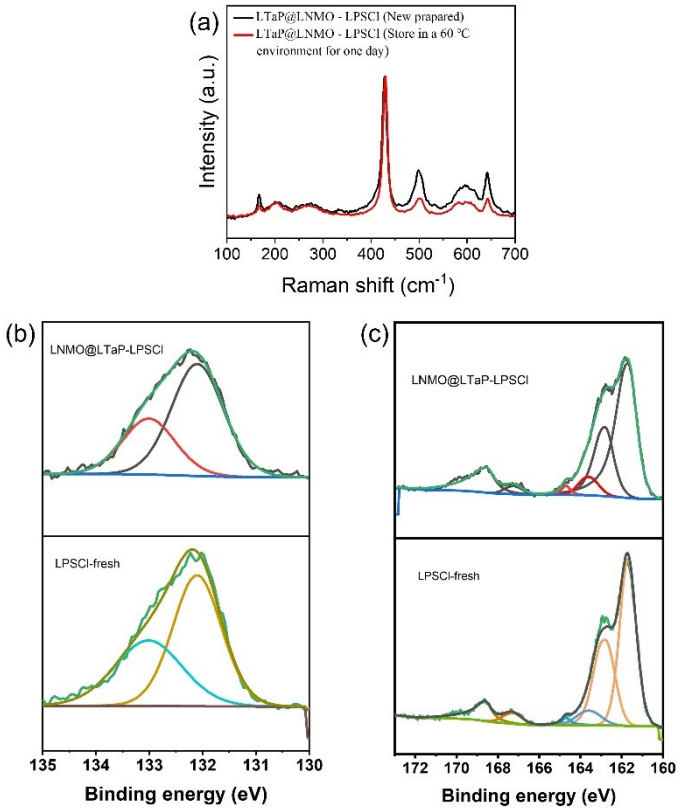

Figure S6. (a) Raman spectra comparison of LTaP@LNMO-LPSCl-VGCF composite cathode before and after standing at 60 ℃ for 24 h. XPS spectra of (b) S2p and (c) P2p of fresh LPSCl and the mixture of LNMO@LTaP and LPSCl after standing for month.

For the coated LNMO, the Raman spectrum of the composite cathode sample after heat treatment shows that the characteristic peak of the PS_4^{3-} group of LPSCl at around 420 cm^{-1} does not change significantly. This indicates that the possible chemical reaction resulting from the contact between the LPSCl and LTa@LNMO does not cause the severe decomposition of LPSCl

LNMO@LTaP and LPSCl were thoroughly ground and mixed, followed by tablet pressing. Subsequently, the samples were stored in a glove box for one month. Comparative analysis of XPS spectra between the treated composite cathode and the fresh LPSCl revealed no significant side reactions occurring between the coated LNMO and LPSCl. This finding provides robust evidence for the stability of LTaP coating layer with LPSCl.

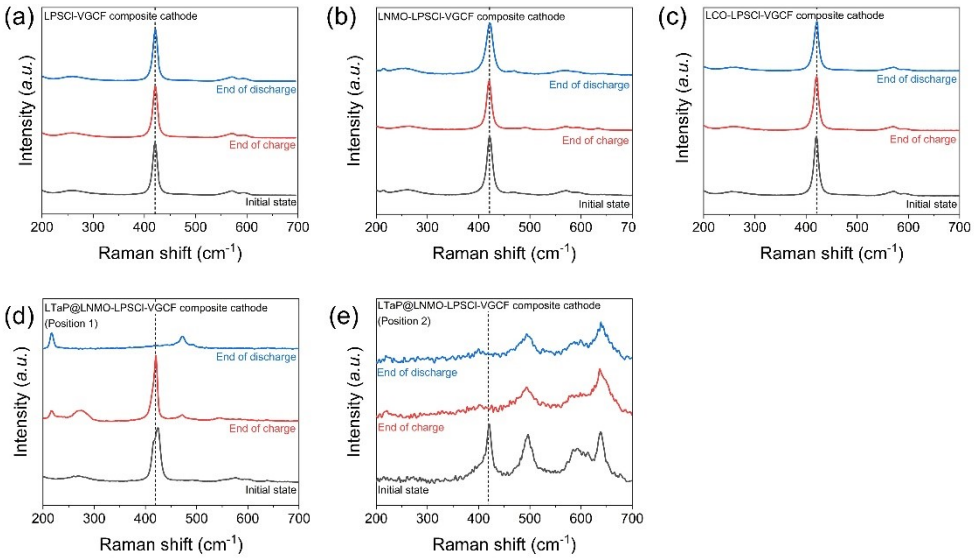

Figure S7. Raman spectra of four composite cathodes at initial state, end of charge, and end of discharge, respectively. (a) LPSCl-VGCF, (b) LNMO-LPSCl-VGCF, (c) LCO-LPSCl-VGCF, and (d, e) LTaP@LNMO-LPSCl-VGCF composite cathodes.

Table S3 The specific values of the peak area and full width at half maximum changes of peak at 424 cm^{-1} in Figure S7 (a-d).

Composite Cathode	**States**	**Peak area (a.u.)**	**FWHM (cm^{-1})**
LPSCl-VGCF	Initial state	23772.95	11.37
	End of charging	23659.35	11.39
LNMO-LPSCl-VGCF	Initial state	21244.05	13.12
	End of charging	16293.81	11.90
LCO-LPSCl-VGCF	Initial state	22154.50	10.72
	End of charging	21204.22	11.18
LTaP@LNMO-LPSCl-VGCF	Initial state	10978.94	17.59
	End of charging	46670.30	21.15

Compared with other battery systems, the charged LTaP@LNMO system showed obvious increase of peak area and FWHW located at 424 cm^{-1} (corresponding to the $\upsilon_s(PS_4^{3-})$), indicating the increased polarization intensity of PS_4^{3-}. This further illustrates the influence of high voltage and high ionic flux on the polarization of PS_4^{3-} group in the LTaP@LNMO system.

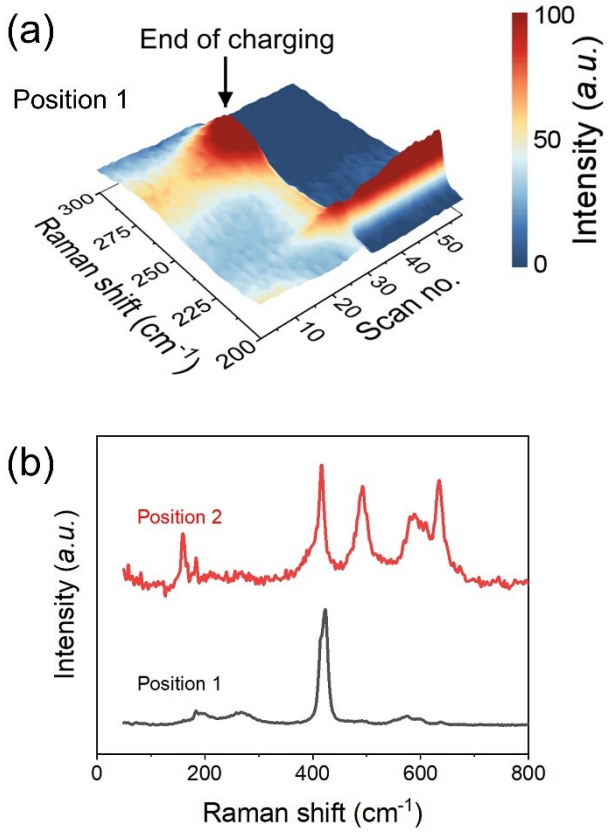

Figure S8. (a) The in-situ Raman results of LTaP@LNMO-LPSCl-VGCF | LPSCl | InLi cell from three dimensional views in Raman shift range of 200~300 cm^{-1}. (b) The ex-situ Raman spectrum of bulk phase of LPSCl (Position 1) and LTaP@LNMO/LPSCl interface (Position 2) in LTaP@LNMO-LPSCl-VGCF composite cathode.

Figure S8a shows that as the charging process progresses, the peak near 270 cm^{-1}, corresponding to the deformation vibration of S–P–S in PS_4^{3-}, shifts towards higher wavenumbers. Moreover, the peak intensity increases, and the full width at half maximum also continuously expands. This indicates that the degree of distortion or amorphization of the PS_4^{3-} group is deepening. Figure S8b shows the basis for our judgment of the near-surface region (Position 2) and the far-surface region (the bulk electrolyte phase, Position 1) of the cathode material. As can be seen from the Raman spectrum of Position 1, the spectral peak intensity of LPSCl at this position is extremely strong, and the characteristic peaks related to LNMO are hardly visible. So, Position 1 is clearly representing the bulk phase LPSCl within the composite cathode, where the content of LPSCl is relatively high.

In contrast, at Position 2, only the characteristic peaks related to LNMO are basically visible, indicating that the content of LPSCl at this position is very low. Consequently, the information of LPSCl about structure and reactions at the LNMO surface can be better obtained from the Position 2.

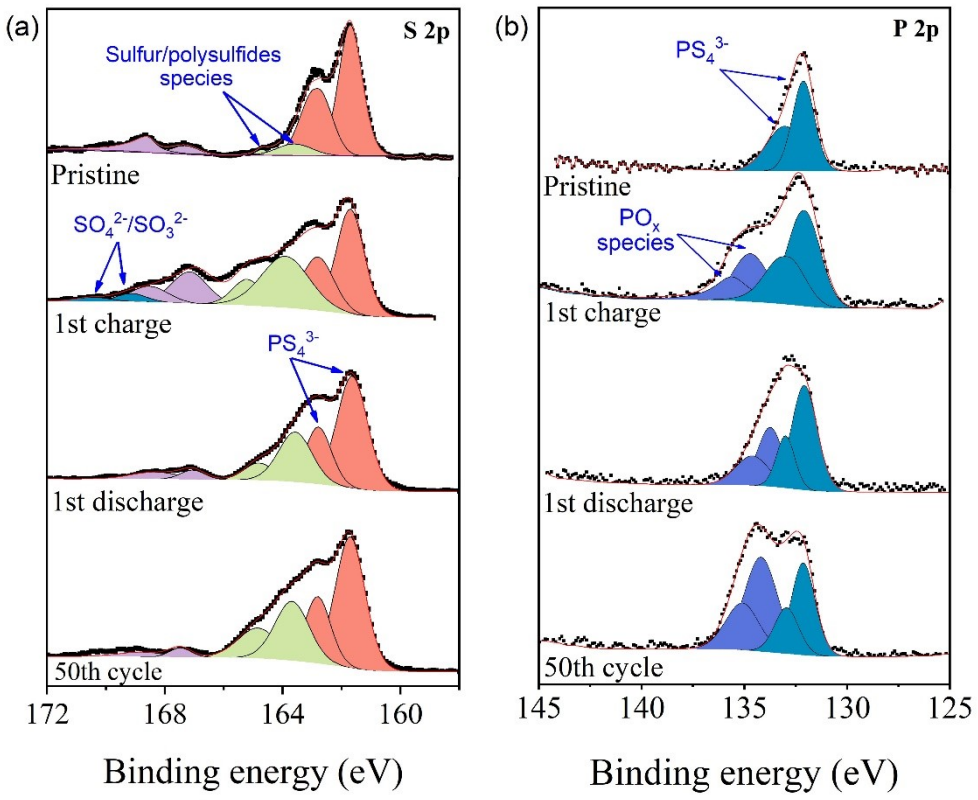

Figure S9. (a) S 2p and (b) P 2p XPS profiles of composite cathode at different states in the LTaP@LNMO-LPSCl-VGCF | LPSCl | InLi cell, respectively.

Table S4 The ratio changes of the peak areas related to S–O/P–O type products to that of PS_4.

	$S–O/PS_4$	$P–O/PS_4$
Pristine	0.38	
1st charge	0.45	0.38
1st discharge	0.11	0.65
50^{th} cycle	0.08	1.26

In the initial composite cathode, we detected two additional peaks near the high binding energy range (167–169 eV), which can be attributed to certain oxygen-containing sulfates ($–SO_x$). This is likely due to the incorporation of O_2 during the preparation of the electrolyte, leading to partial decomposition of LPSCl as shown in Figure S9. During the 1st charging process, we detected the appearance of Li_2S and S. Meanwhile, the content of sulfates ($–SO_x$) also increased. However, at the end of the 1st discharging process, it seemed that the PS_4^{3-} returned to its original state again. Moreover, the results after the 50th cycle show that LPSCl was not completely decomposed, but rather generated a relatively large number of by-products, such as S. Combined with the previous in-situ Raman results, we can speculate that during the electrochemical charge-discharge process,

by-products that inhibit kinetic performance are generated at the interface between the coated LNMO and LPSCl. These by-products include polysulfides or S, as well as a small amount of S–O and P–O by-products. Moreover, the reaction between them is intense. As can be seen from Figure S9, at the end of the 1st charging state, relatively obvious by-products were generated. Among them, P–O species, after being produced in the first cycle, showed a significant cumulative effect as the cycling continued. The XRD test results of the composite cathode after the 50th cycle (Figure S10) indicate that the presence of P–O species is quite evident. A clear XRD pattern comparison between composite cathode and LNMO@LTaP powder shows that the signal of P–O products does not come from the coating layer. This indicates that these by-products result from the continuous decomposition of the solid-state electrolyte during the cycling process. This cumulative phenomenon indicates that these by-products can exist stably at high voltages. Meanwhile, being poor conductors of electrons and ions, the consequence of their accumulation is the poor kinetic performance at the interface. The $–SO_x$ species, which showed a significant increase during the first-cycle charging process, decreased after the first-cycle discharging. After the 50th cycle, the amount of $–SO_x$ species became even less, and it was difficult to observe the corresponding characteristic peaks in the XRD pattern in Figure S10. The accumulation of P–O species, characterized by their electronic insulating properties and poor ionic conductivity, exerts a suppressive effect on the electrochemical performance, which is the main reason for the continuous decline in the cycling performance of the coated LNMO all-solid-state battery.

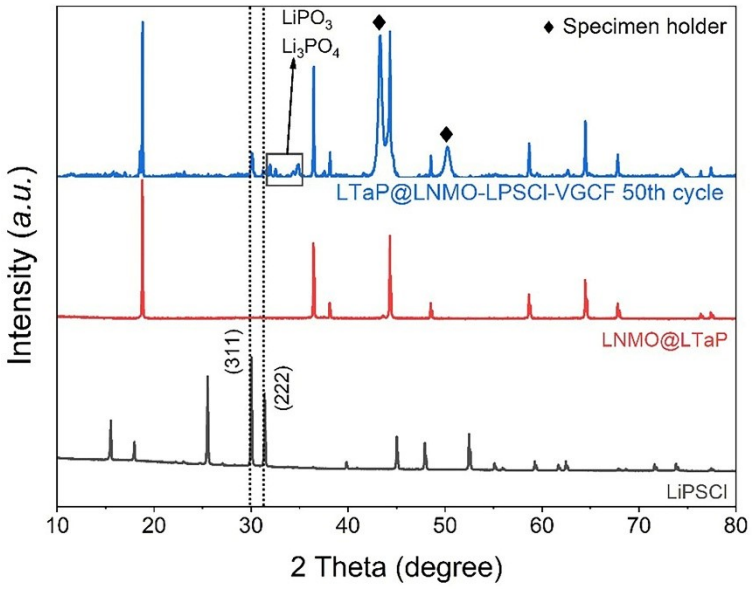

Figure S10. The comparison of XRD patterns between original LPSCl, LTaP@LNMO cathode powders, and LTaP@LNMO-LPSCl-VGCF composite cathode after 50 cycles.

References:

1 Yubuchi S, Teragawa S, Aso K, et al. Preparation of high lithium-ion conducting LPSCl solid electrolyte from ethanol solution for all-solid-state lithium batteries. *Journal of Power Sources*, 2015, **293**: 941-945.

2 Zhang J, Zheng C, Li L, et al. Unraveling the Intra and Intercycle Interfacial Evolution of LPSCl - Based All-Solid-State Lithium Batteries. *Advanced Energy Materials*, 2020, **10**(4): 1903311.

3 Zhou Y, Doerrer C, Kasemchainan J, et al. Observation of Interfacial Degradation of LPSCl against Lithium Metal and $LiCoO_2$ via In Situ Electrochemical Raman Microscopy. *Batteries & Supercaps*, 2020, **3**(7): 647-652.

4 Sang L, Haasch R T, Gewirth A A, et al. Evolution at the Solid Electrolyte/Gold Electrode Interface during Lithium Deposition and Stripping. Chemistry of Materials, 2017, **29**(7): 3029-3037.

5 Choi S, Ann J, Do J, et al. Application of Rod-Like LPSCl Directly Synthesized by a Liquid Phase Process to Sheet-Type Electrodes for All-Solid-State Lithium Batteries. *Journal of The Electrochemical Society*, 2019, **166**: A5193-A5200.

6 Wang S, Zhang Y, Zhang X, et al. High-Conductivity Argyrodite LPSCl Solid Electrolytes Prepared via Optimized Sintering Processes for All-Solid-State Lithium–Sulfur Batteries. *ACS Applied Materials & Interfaces*, 2018, **10**(49): 42279-42285.

7 Maniwa R, Calpa M, Rosero-Navarro N C, et al. Synthesis of sulfide solid electrolytes from Li_2S and P_2S_5 in anisole. *Journal of Materials Chemistry A*, 2021, **9**(1): 400-405.

8 Tachez M, Malugani J-P, Mercier R, et al. Ionic conductivity of and phase transition in lithium thiophosphate Li_3PS_4. *Solid State Ionics*, 1984, **14**(3): 181-185.

9 Xu Y-H, Zhao S-X, Deng Y-F, et al. Improved Electrochemical Performance of 5 V Spinel $LiNi_{0.5}Mn_{1.5}O_4$ Microspheres by F-doping and Li_4SiO_4 coating. *Journal of Materiomics*, 2016, **2**.

10 Amdouni N, Zaghib K, Gendron F, et al. Structure and insertion properties of disordered and ordered $LiNi_{0.5}Mn_{1.5}O_4$ spinels prepared by wet chemistry. *Ionics*, 2006, 12(2): 117-126.

11 Xue Y, Wang Z, Yu F, et al. Ethanol-assisted hydrothermal synthesis of $LiNi_{0.5}Mn_{1.5}O_4$ with excellent long-term cyclability at high rate for lithium-ion batteries. *Journal of Materials Chemistry A*, 2014, **2**(12): 4185-4191.